Journal of Advanced Ceramics
2022, **11**(5): 769–783
https://doi.org/10.1007/s40145-022-0570-x
ISSN 2226-4108
CN 10-1154/TQ

Research Article

Precise control of surface oxygen vacancies in ZnO nanoparticles for extremely high acetone sensing response

Jihyun LEE[a,†], Youngmoon CHOI[b,†], Byoung Joon PARK[c], Jeong Woo HAN[c,d], Hyun-Sook LEE[a,*], Jong Hyeok PARK[b,*], Wooyoung LEE[a,*]

[a]*Department of Materials Science and Engineering, Yonsei University, Seoul 03722, Republic of Korea*
[b]*Department of Chemical and Biological Engineering, Yonsei University, Seoul 03722, Republic of Korea*
[c]*Department of Chemical Engineering, Pohang University of Science and Technology, Pohang 37673, Republic of Korea*
[d]*Institute for Convergence Research and Education in Advanced Technology, Yonsei University, Seoul 03722, Republic of Korea*

Received: September 29, 2021; Revised: December 20, 2021; Accepted: January 11, 2022

Abstract: ZnO has been studied intensely for chemical sensors due to its high sensitivity and fast response. Here, we present a simple approach to precisely control oxygen vacancy contents to provide significantly enhanced acetone sensing performance of commercial ZnO nanopowders. A combination of H_2O_2 treatment and thermal annealing produces optimal surface defects with oxygen vacancies on the ZnO nanoparticles (NPs). The highest response of ~27,562 was achieved for 10 ppm acetone in 0.125 M H_2O_2 treated/annealed ZnO NPs at the optimal working temperature of 400 ℃, which is significantly higher than that of reported so far in various acetone sensors based on metal oxide semiconductors (MOSs). Furthermore, first-principles calculations indicate that pre-adsorbed O formed on the surface of H_2O_2 treated ZnO NPs can provide favorable adsorption energy, especially for acetone detection, due to strong bidentate bonding between carbonyl C atom of acetone molecules and pre-adsorbed O on the ZnO surface. Our study demonstrates that controlling surface oxygen vacancies by H_2O_2 treatment and re-annealing at optimal temperature is an effective method to improve the sensing properties of commercial MOS materials.

Keywords: gas sensors; acetone; metal oxide semiconductors (MOSs); ZnO nanoparticles (NPs); H_2O_2 treatment

1 Introduction

Monitoring environmental acetone indoor and outdoor for safety or breath acetone for non-invasive diagnosis has increased with increasing interest in health care [1]. Acetone, one of the volatile organic compounds (VOCs), is a hazardous gas that is widely used in industrial, laboratory, and domestic areas, causing indoor and outdoor environmental pollution and risking human health. Acetone with a concentration higher than 173 ppm damages not only the skin, throat, nose, and eyes but also the central nervous system [2]. The recommended occupational threshold value for acetone

† Jihyun Lee and Youngmoon Choi contributed equally to this work.
* Corresponding authors.
E-mail: H.-S. Lee, h-slee@yonsei.ac.kr;
J. H. Park, lutts@yonsei.ac.kr;
W. Lee, wooyoung@yonsei.ac.kr

has been set to 250 ppm considering an 8 h time-weighted average [3]. Additionally, acetone is highly flammable owing to its high volatility even at room temperature [4]. Therefore, monitoring the acetone concentration in the environment is a critical issue. Furthermore, acetone is produced in the human body through metabolic processes and released through exhaled breath. A high concentration of breath acetone can be released due to diabetes [5], fat metabolism [6], and heart failure [7,8]. The breath acetone concentration ranges from 0.3 to 0.9 ppm for healthy people [5,6], but it is over 1.8 ppm for diabetes patients [5,6] and over 40 ppm for a person on a ketogenic diet [6,9]. Therefore, breath acetone can be used as a biomarker to diagnosis-related diseases such as diabetes, obesity, and systolic dysfunction.

The concentration of acetone in air or breath has been commonly measured by several techniques based on gas chromatography and mass spectrometry. These systems precisely measure the concentration; however, they are bulky, complex, time-consuming, and expensive [1]. Additionally, skilled operators are required, and gas samples must be collected before the measurement for the analysis. Resistive gas sensors based on metal oxide semiconductors (MOSs) are considered as an alternative. Among various MOS sensing materials, ZnO has been studied intensively due to its several advantages. It is chemically and thermally stable, and its various forms of nanostructure can be fabricated at a low cost. Moreover, it has favorable sensing properties such as high sensitivity and fast response.

To improve the sensing properties of ZnO, various approaches have been reported including nanostructuring [10–12], transition metal doping [13,14], and noble metal loading [15,16]. Additionally, the control of the surface defect [17] has been alternatively proposed because the MOS sensor response is highly dependent on the surface chemistry. The surface defect can be introduced during material synthesis [18,19] or subsequent annealing treatment [20,21]. Especially, oxygen vacancies, among various defects, of nanostructured ZnO play an important role in improving the sensing properties because they act as the electron donors and promote the ionization and chemisorption of oxygen molecules on the ZnO surface [17,18]. Hence, adsorbed oxygen ion species are easily generated on the surface of more oxygen-vacant ZnO, enhancing the sensing response significantly. It has been suggested that the number of oxygen vacancies of ZnO can be increased using a simple method of H_2O_2 surface treatment and annealing [22,23]. The as-grown ZnO film and ZnO nanorods exhibited slightly enhanced sensing response compared to their untreated counterparts to detect ethanol due to the application of the surface treatment [24]. Therefore, more precisely controlled oxygen vacancy formation in ZnO is expected to be an effective strategy to improve the sensing properties of ZnO as a chemical sensor.

In this study, we found that the acetone sensing properties of commercial ZnO nanopowders were increased unprecedently via two consecutive steps: optimal H_2O_2 solution treatment and stabilization by thermal annealing. ZnO powder-based sensors which are treated by the optimal H_2O_2 concentration and high-temperature annealing showed a tremendously high sensing response from more than ~27,000 to 10 ppm acetone, which is significantly higher than that reported so far for the MOS-based various acetone sensors. The sensing mechanism of the greatly enhanced response is described by the effect of surface oxygen vacancies through the analysis of surface chemistry and simulation.

2 Materials and methods

2.1 Preparation of oxygen-vacant ZnO nanoparticles (NPs)

Commercial ZnO nanopowders were used to prepare the oxygen vacancies on the surface of ZnO NPs. First, 300 mg of commercial ZnO nanopowders (< 50 nm, 97%, Sigma Aldrich) were dissolved into 80 mL of deionized water. Furthermore, the dissolved solution was stirred for 1 h at 75 ℃. After that, 50 wt% of different concentrations of hydrogen peroxide (H_2O_2) solution (Sigma Aldrich) was poured into the mixed solution and maintained for 2 h at 75 ℃ under continuous stirring. The H_2O_2 aqueous solution was prepared with the following concentrations using deionized water: 0.075, 0.125, 0.25, and 1 M. The resultant white precipitate was washed with deionized water, separated by centrifugation at 11,000 rpm, and then dried at room temperature. The as-obtained ZnO_2 powders were annealed in air atmosphere for 2 h at 400 ℃ for transforming it into oxygen-deficient ZnO nanopowders with a pale yellow color.

2.2 Characterization of sensing materials

The crystal structures and morphology of the prepared

powders were characterized by the X-ray diffractometer (Ultima IV, Rigaku) with Cu Kα radiation (1.5406 Å) and the high-resolution transmission electron microscope (JEM-ARM 200F, JEOL), respectively. The chemical states of the sample surface were investigated using the X-ray photoelectron spectroscope (K-alpha, Thermo Scientific Incorp.) with Al Kα source (1486.6 eV). Moreover, the X-ray photoelectron spectroscopy (XPS) results were calibrated by adventitious carbon C 1s peak at 285 eV. Raman spectra were measured by Horiba Jobin Yvon HR800 UV with Ar^+ laser excitation of 488 nm to understand chemical states further.

2. 3 Fabrication of sensor devices

Interdigitated Pt electrodes were patterned on a SiO_2/Si substrate (8.5 mm × 8.5 mm) using photolithographic technique after depositing Pt layer (100 nm) using a direct current (DC) magnetic sputtering system to fabricate the sensor devices. The Cr layer (20 nm) was deposited to provide good adhesion Pt layer and the substrate. The as-prepared nanopowders were mixed with an α-terpineol binder; and the mixtures were spread on the interdigitated Pt electrodes. The sensor device was annealed at 600 ℃ in a nitrogen environment for 1 h to remove the binding agent and enhance the stability of the sensor.

2. 4 Gas sensing measurements

The sensing performance of the H_2O_2 treated and annealed ZnO NPs for acetone was tested with a customized sensing measurement system. The sensor device was mounted on a chamber of tube furnace equipped with a gas flow system connected with mass flow controllers (MFCs) and gas cylinders. Furthermore, the acetone concentration was controlled by adjusting the flow rate between the high concentration of acetone and synthetic air of a balance gas. The adjusted amount of acetone and synthetic air was injected into the senor chamber at 100 sccm of a constant flow rate. The operating temperature of the sensor was controlled using a temperature controller of the tube furnace. The sensing performance of the samples was examined in the temperature range of 300–500 ℃. Moreover, the electric sensing response of the samples was measured using a nanovoltmeter (Keithley 2182) at 10 nA of a constant current with a time interval of 1 s using a current source (Keithley 6220). The sensing response was defined as $\Delta R/R_g$, where $\Delta R = R_a - R_g$, R_a and R_g represent the resistance in air and acetone gas, respectively.

2. 5 Computational details

We performed first-principles calculations considering spin-polarized density functional theory using the Vienna *ab initio* Simulation Package [25,26] and projected augmented wave (PAW) potentials [27,28]. Perdew–Burke–Ernzerhof (PBE) functional using the generalized gradient approximation (GGA) was considered for electronic exchange and correlation [29]. All calculations used a plane-wave basis set with a cutoff of 500 eV. The convergence threshold for total energy calculations was set at 10^{-4} eV. All geometry optimizations were conducted using a conjugate gradient algorithm considering the forces acting on each atom and terminated when they converged within 0.03 eV/Å for electronic relaxation. The *k*-point sampling of the Brillouin zone was used with a 3 × 3 × 1 Monkhorst–Pack grid [30]. We obtained the bulk ZnO parameters: $a = b = 3.289$ Å and $c = 5.307$ Å, which agree very well with the previous experimental data ($a = b = 3.250$ Å and $c = 5.207$ Å) [31]. The slab models representing the ZnO($10\bar{1}0$) surface consisted of three ZnO double-layers separated by approximately 18 Å vacuum regions. In all cases, the atoms in the bottom ZnO double layer were fixed for simulating the underlying bulk structure. The calculations for gas-phase molecules were performed in a 20 Å × 21 Å × 22 Å supercell.

3 Results and discussion

To characterize the crystal structure modification of the commercial ZnO NPs by the H_2O_2 treatment and the subsequent thermal annealing, the X-ray diffraction (XRD) measurements were conducted as shown in Fig. 1. It shows the XRD patterns of (1) pure ZnO NPs, (2) ZnO NPs after 1 M H_2O_2 treatment, and (3) ZnO NPs after 1 M H_2O_2 treatment followed by thermal annealing. The ZnO NPs with a hexagonal wurtzite structure (JCPDS No. 36-1451) were easily transformed into the ZnO_2 cubic phase (JCPDS No. 76-1364) after 1 M H_2O_2 treatment due to Reaction (1) (Fig. 1) [24]. The diffraction peaks of the annealed samples after 1 M H_2O_2 treatment were well-indexed to the crystal structure of the ZnO phase without any impurities and secondary phases. However, it releases oxygen by

thermal decomposition at a temperature above 200 ℃, and easily converts to a more stable phase, ZnO, at high temperatures (Reaction (2)) [24]. Particularly, oxygen vacancies were formed on the surface of ZnO during its transformation from ZnO_2 to ZnO [24].

$$ZnO + H_2O_2 \rightarrow ZnO_2 + H_2O \quad (1)$$

$$2ZnO_2 \xrightarrow{\text{Annealing}} 2ZnO + O_2 \quad (2)$$

The XRD results indicated that the crystal structure of the ZnO NPs changed to cubic ZnO_2 phase during H_2O_2 treatment, and returned to the hexagonal ZnO phase after annealing at 400 ℃. Hence, the surface of ZnO particles was damaged presumably during the H_2O_2 treatment and re-annealing step, forming surface defects [24].

We prepared various ZnO NPs that were annealed at 400 ℃ after H_2O_2 treatments with different molar concentrations (x M) to investigate the effect of H_2O_2 on the sensing performance of the final ZnO product. The crystalline phase of these NPs was compared to that of pure ZnO. Figure 2(a) shows the XRD spectra

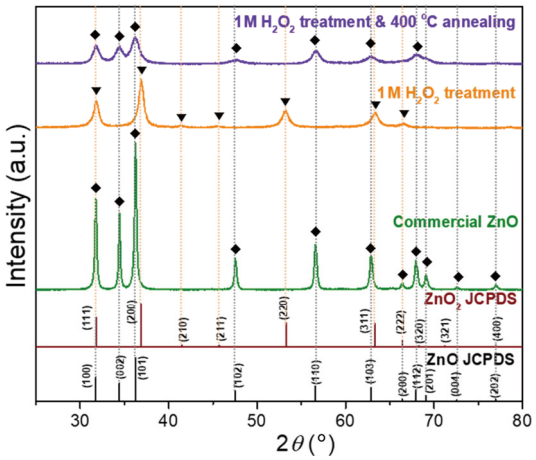

Fig. 1 XRD patterns of commercial ZnO, 1 M H_2O_2 treated ZnO, and 1 M H_2O_2 treated/annealed ZnO. Standard XRD patterns of hexagonal wurtzite ZnO (JCPDS No. 36-1451) and cubic ZnO_2 (JCPDS No. 76-1364) are shown as vertical lines at the bottom.

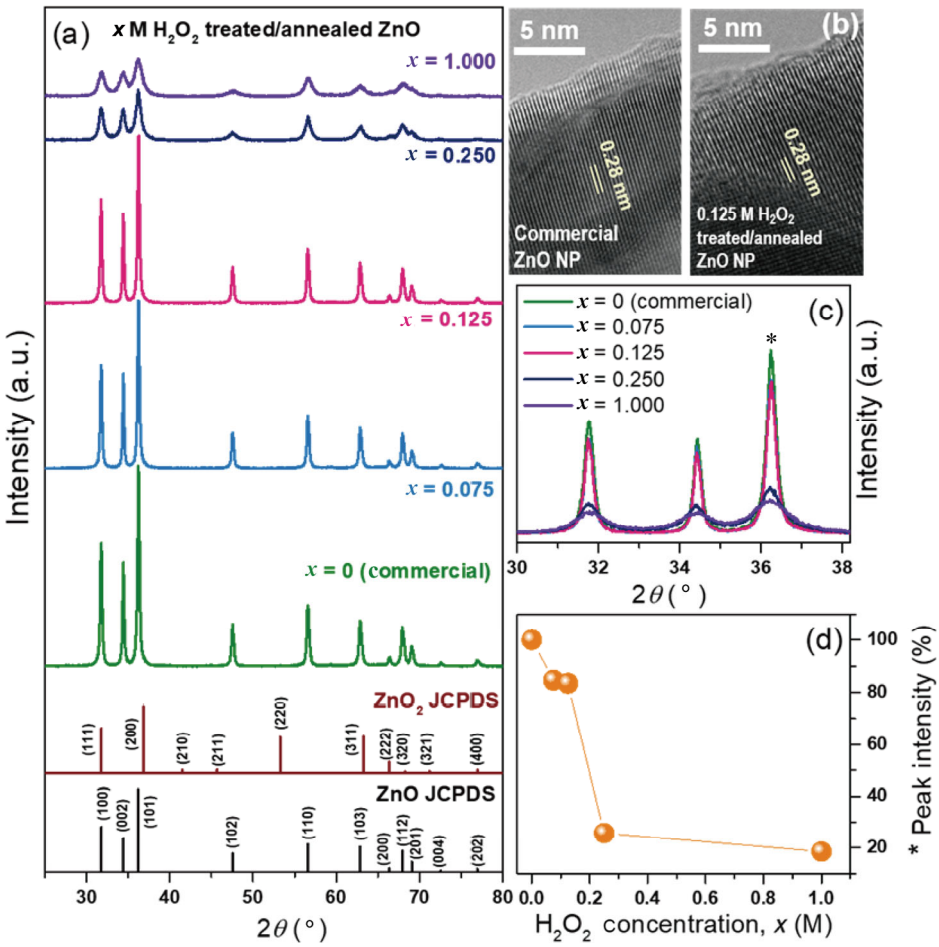

Fig. 2 (a) XRD patterns of commercial ZnO and x M H_2O_2 treated/annealed ZnO (x = 0.075, 0.125, 0.250, and 1.000) nanopowders. (b) TEM image of commercial ZnO NP (left) and 0.125 M H_2O_2 treated/annealed ZnO NP (right). (c) Magnified three main peaks of the prepared ZnO samples. (d) Intensity of the first main peak (*) as a function of H_2O_2 concentration.

of the pure ZnO and x M H_2O_2 treated/annealed ZnO (x = 0.075, 0.125, 0.250, and 1.000) NPs. All the prepared NPs have the hexagonal ZnO phase (Fig. 2(a)). Figure 2(b) shows the high-resolution transmission electron microscopy (HR-TEM) image of ZnO NP (left) and 0.125 M H_2O_2 treated/annealed ZnO NPs (right). Both images show clear lattice fringes with an interplanar spacing of approximately 0.28 nm, ascribing to the (100) plane in the hexagonal ZnO. However, the overall diffraction peak intensity decreases with the increasing H_2O_2 concentration, x (Figs. 2(a) and 2(c)). The intensity of the main peak (*) was compared to that of the pure ZnO NPs. As shown in Fig. 2(d), the peak intensity slightly decreases at 0.125 M compared to that of the pure ZnO; however, it is abruptly decreased at 0.250 M. Additionally, the sharp diffraction peaks broadened from 0.250 M (Fig. 2(c)), which means a significant decrease in crystallinity at the concentrations of H_2O_2 over 0.250 M. We found that the particle size decreases for H_2O_2 concentrations above 0.250 M from the broadening of the diffraction peaks.

We calculated the crystallite size of the as-prepared nanopowders using the Halder–Wagner method as follows:

$$\left(\frac{\beta\cdot\cos\theta}{\sin\theta}\right)^2=\frac{K\lambda}{D}\frac{\beta}{\tan\theta\cdot\sin\theta}+16\varepsilon^2 \qquad (3)$$

where θ is the Bragg angle, D represents the crystallite size, β denotes the peak width at half-maximum intensity, K is the crystallite configuration constant, λ is the wavelength of Cu Kα radiation, and ε denotes the weighted average strain [32]. The Halder–Wagner method gives more weight to the diffraction peaks at low and intermediated angle ranges [33]. The estimation results were more accurate than various other crystallite size estimation methods for the spherical metal-oxide NPs, such as CeO_2 and TiO_2 [33,34]. The crystallite size can be determined from the slope of $(\beta/\tan\theta)^2$ vs. $\beta/(\tan\theta\cdot\sin\theta)$ plot [33]. The Halder–Wagner plots for all the prepared samples after adopting the K = 4/3 for the volume-weighted average size of spherical crystallites [33] are shown in Figs. 3(a)–3(e). The calculated crystallite sizes are summarized in Fig. 3(f). The sizes of the commercial ZnO NPs and 0.075 and 0.125 M treated/annealed ZnO NPs were both in the range of 52–55 nm, and they were significantly reduced to ~19 and ~11 nm for 0.250 and 1.000 M treated/annealed ZnO NPs, respectively. These outcomes are in good agreement with the results obtained from the TEM analysis provided in Figs. 4(a)–4(e).

Furthermore, we analyzed the reason for the size reduction at high concentrations of H_2O_2. ZnO NPs changed to ZnO_2 NPs during H_2O_2 treatment (Reaction (1)) according to the phase transformation mechanism. Moreover, ZnO_2 NPs reversed to ZnO NPs with O_2^{2-}

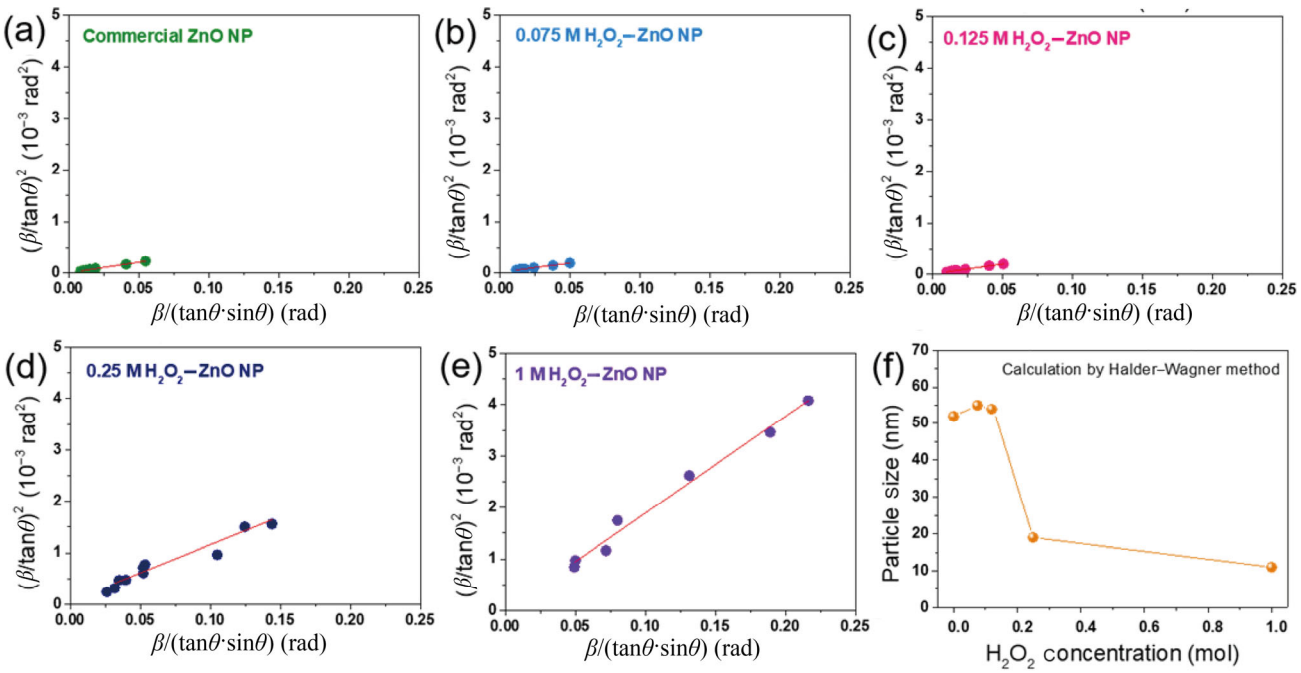

Fig. 3 Halder–Wagner plots of (a) commercial ZnO NPs, (b) 0.075 M H_2O_2 treated/annealed ZnO NPs, (c) 0.125 M H_2O_2 treated/annealed ZnO NPs, (d) 0.25 M H_2O_2 treated/annealed ZnO NPs, and (e) 1 M H_2O_2 treated/annealed ZnO NPs. (f) Crystalline size estimated from the slope of the linear fit.

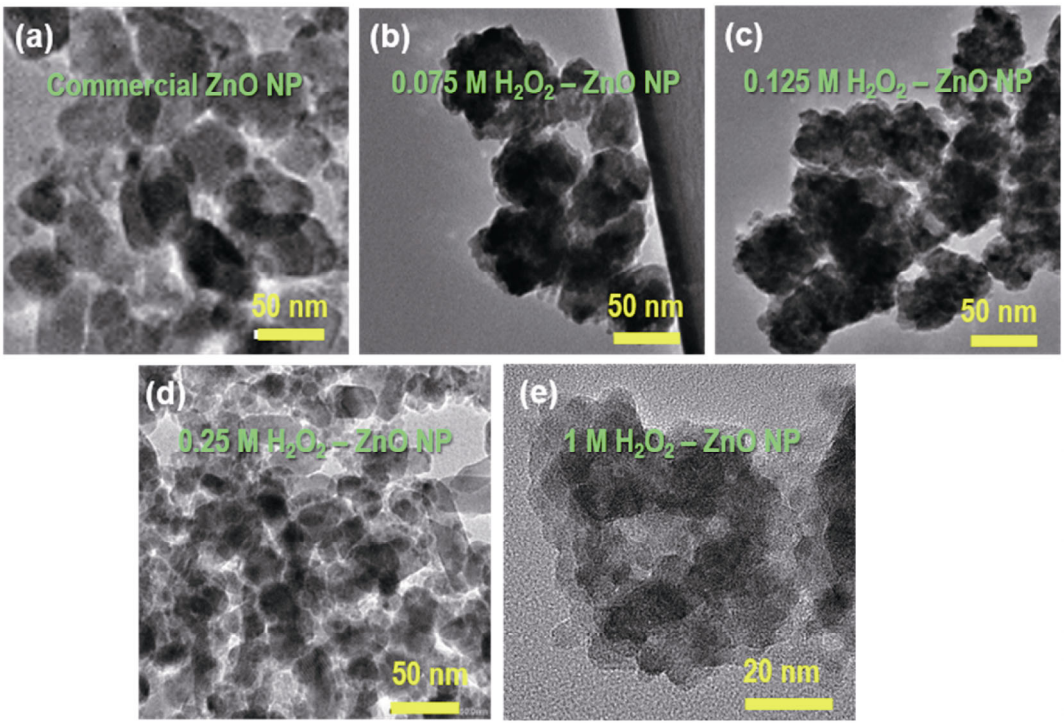

Fig. 4 TEM images of (a) commercial ZnO NPs, (b) 0.075 M H_2O_2 treated/annealed ZnO NPs, (c) 0.125 M H_2O_2 treated/annealed ZnO NPs, (d) 0.25 M H_2O_2 treated/annealed ZnO NPs, and (e) 1 M H_2O_2 treated/annealed ZnO NPs.

decomposition during annealing at 400 ℃ (Reaction (2)). Therefore, the particle size can be reduced during this transformation from ZnO_2 to ZnO. Highly concentrated H_2O_2 excessively oxidizes ZnO NPs, transforming them into ZnO_2, and decomposes large amount of O_2^{2-} in the subsequent annealing process, resulting in a significant size reduction. We investigated the size change of ZnO NPs based on various H_2O_2 concentrations after H_2O_2 treatment and annealing using scanning electron microscopy (SEM). The 0.125 M H_2O_2 treated (Fig. S2(b) in the Electronic Supplementary Material (ESM)) and annealed ZnO NPs (Fig. S2(d) in the ESM) show sizes similar to those of the commercial ZnO NPs (Fig. S2(a) in the ESM). However, the size of 1.000 M particles did not change compared to that of the commercial one after H_2O_2 treatment (Fig. S2(c) in the ESM); however, it decreased significantly after the annealing process (Fig. S2(e) in the ESM). It was seen that the small-sized particles of ~10 nm were aggregated into particles with an average size of ~55 nm. The size obtained from the SEM image agreed well with the results obtained from the XRD (Fig. 2) and TEM (Fig. 4) analyses. Therefore, the significant size reduction at high concentrations of H_2O_2 can be explained by the decomposition of a large amount of O_2^{2-} from the excessively oxidized ZnO_2 that was converted to ZnO during the annealing process.

The sensing performance of the pure ZnO NPs was measured after exposing them to acetone at different concentrations (0.01–10 ppm) or at different operating temperatures (300–500 ℃). Figure 5(a) shows a representative plot of variation in sensing responses of the 0.125 M H_2O_2 treated/annealed ZnO NPs to 10 ppm acetone at different operating temperatures. Figure 5(b) presents maximum sensing response of the pure ZnO NPs and x M H_2O_2 treated/annealed ZnO NPs (x = 0.075, 0.125, 0.250, and 1.000) as a function of operating temperature. All the samples show their highest response at 400 ℃, implying an optimal operating temperature. Particularly, the highest response for 10 ppm acetone was observed to be ~27,562 from the sample of 0.125 M H_2O_2 treated/annealed ZnO NPs. Additionally, the 0.125 M H_2O_2 treated/annealed ZnO NPs show a fast response time in the range of 1.3–2.6 s at various working temperatures of 300–500 ℃ (see the inset of Fig. 5(a)). The response time was estimated using a definition—the time required to reach 90% of the total change in response. Figure 5(c) shows the variation in sensing response of the 0.125 M H_2O_2 treated/annealed ZnO NPs to different acetone concentrations (0.01–10 ppm) at the optimal operating temperature of 400 ℃. The result indicates that the

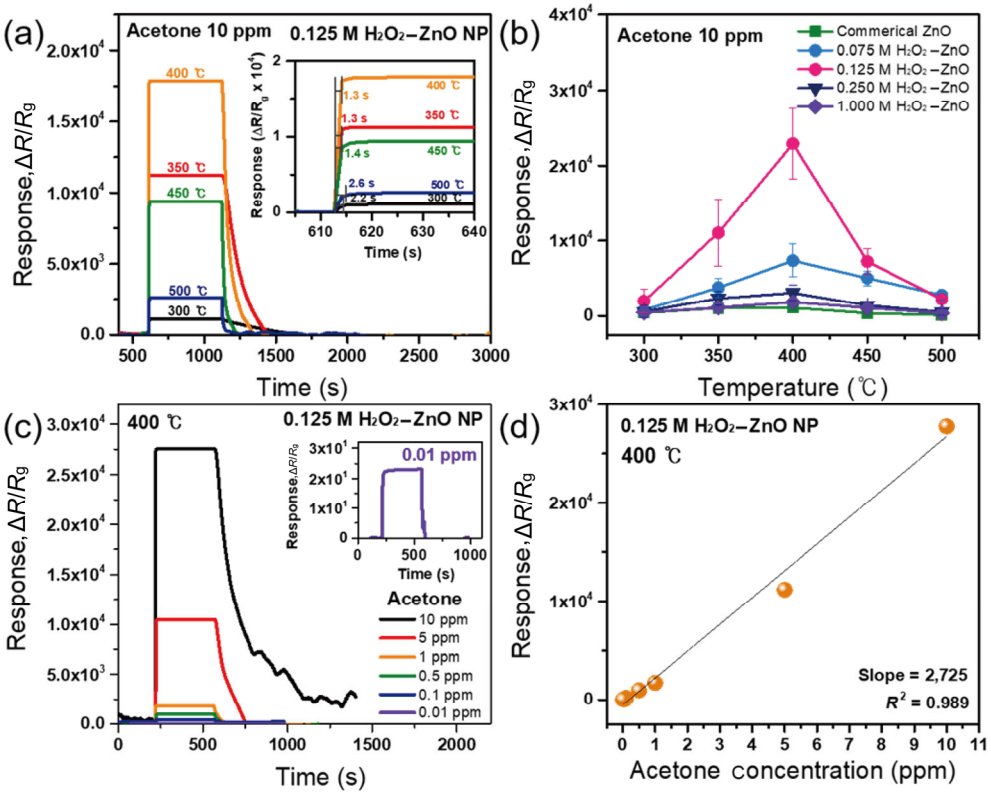

Fig. 5 (a) Variation in the response of 0.125 M H_2O_2 treated/annealed ZnO NPs to 10 ppm acetone in the operating temperatures of 300, 350, 400, 450, and 500 ℃. The inset depicts response time from their sensing curves. (b) Maximum sensing response of commercial ZnO NPs and x M H_2O_2 treated/annealed ZnO NPs (x = 0.075, 0.125, 0.250, and 1.000) at 10 ppm acetone as a function of operating temperature. (c) Variation in the response of the 0.125 M sample at an optimum operating temperature (400 ℃) as a function of acetone concentration. (d) Sensing response of 0.125 M sample to different concentrations of acetone in 0.01, 0.1, 0.5, 1, 5, and 10 ppm at 400 ℃. Sensitivity was calculated from a slope of a linear fit of the response.

sample can detect ultra-low concentration of 0.01 ppm acetone. Figure 5(d) shows the maximum response as a function of acetone concentration. The response has a good linear relationship with acetone concentration (linear correlation coefficient R^2 = 0.989). The sensitivity of the 0.125 M H_2O_2 treated/annealed ZnO NPs for detecting acetone in the range of 0.01–10 ppm was estimated to be approximately 2725 via a slope obtained by linear fitting.

According to the sensing results, the 0.125 M H_2O_2 treated/annealed ZnO NPs exhibited extremely high sensing response for the detection of 10 ppm acetone among the prepared samples. Because the sensing performances are strongly influenced by the chemical states of the metal oxide surface, we performed surface elemental composition analysis by XPS. The chemical states of the sample surface were analyzed by probing the Zn 2p and O 1s states. Figure 6(a) shows the XPS spectra of the Zn 2p state for all samples. All samples show two main peaks corresponding to the electronic states of Zn $2p_{1/2}$ (~1044 eV) and Zn $2p_{3/2}$ (~1021 eV), indicating the existence of a divalent oxidation state of Zn atoms in ZnO crystals. Furthermore, we observed that the Zn $2p_{3/2}$ spectrum peak was shifted to the lower binding energy for 0.075 and 0.125 M treated/annealed ZnO NPs, as seen in Fig. 6(b). Additionally, more shift was observed for the 0.125 M samples. The shift of Zn $2p_{3/2}$ peak to lower binding energy is closely related to the existence of oxygen vacancies in ZnO. The binding energies of Zn $2p_{3/2}$ in ZnO were decreased with an increasing concentration of oxygen vacancies [35].

The existence of oxygen vacancies in the as-prepared ZnO NPs was analyzed by the detailed characterization of the O 1s state in the XPS spectra. Figures 6(c)–6(g) show that the O 1s peaks are deconvoluted into three distinct Gaussian peaks centered at ~530, ~531, and ~532 eV. These peaks are associated with O^{2-} ions of Zn–O bonds in the ZnO wurtzite (O-lattice), the adsorbed oxygen ions, O^-, and O^{2-} in the oxygen-deficient regions within ZnO (O-deficient), and the chemisorbed

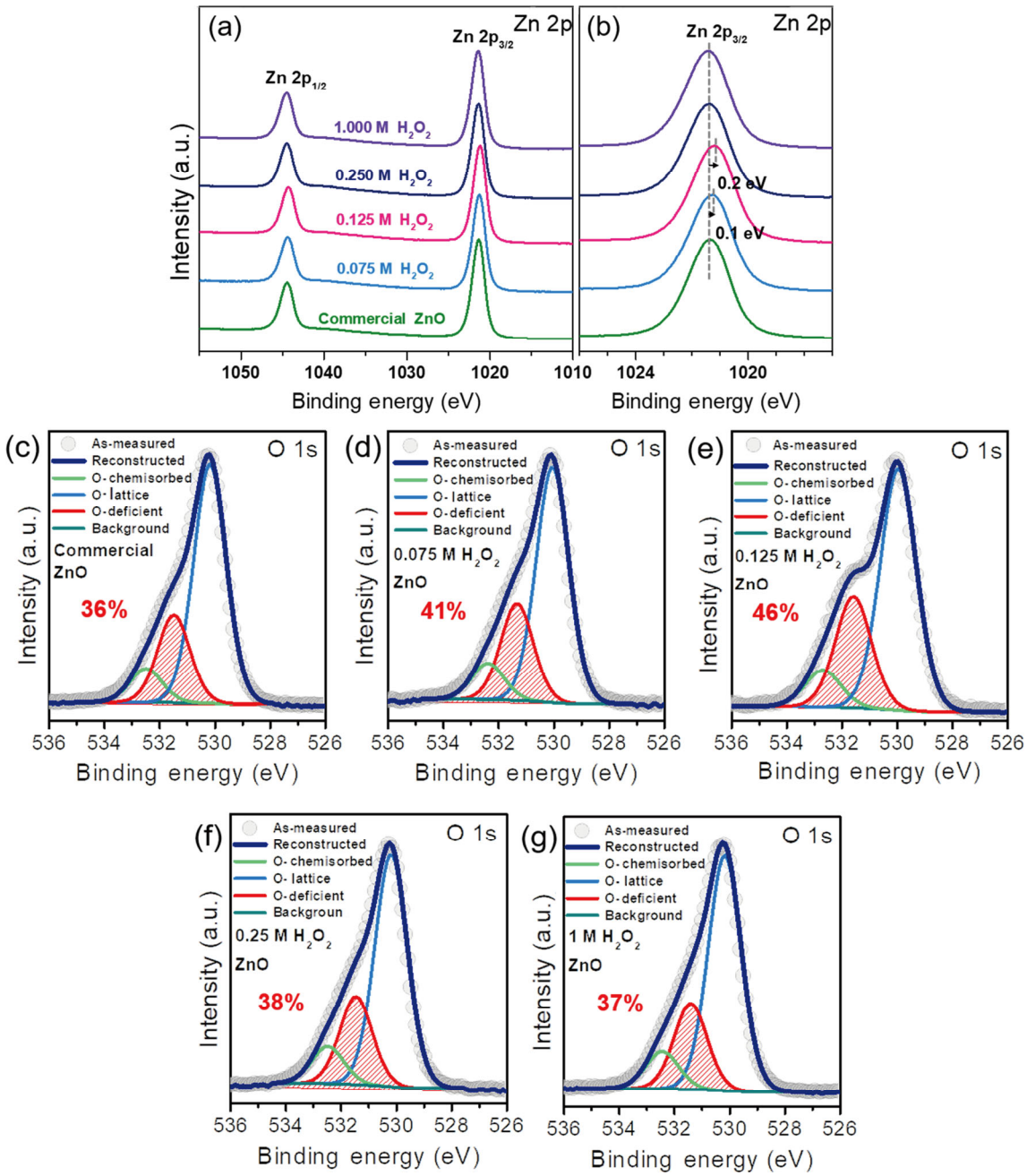

Fig. 6 (a) Zn 2p XPS spectra of commercial ZnO NPs and *x* M H_2O_2 treated/annealed ZnO NPs (*x* = 0.075, 0.125, 0.250, and 1.000); (b) Zn $2p_{3/2}$ peaks of the samples; O 1s XPS spectra of (c) commercial ZnO NPs and (d–g) *x* M H_2O_2 treated/annealed ZnO NPs: (d) *x* = 0.075, (e) *x* = 0.125, (f) *x* = 0.250, and (g) *x* = 1.000.

oxygen species, such as adsorbed O_2 and H_2O on the surface of ZnO (O-chemisorbed) [36]. Among the three different types of oxygen states, the O-deficient state is considered to be directly related to the sensing performance [37]. The number of oxygen vacancies was estimated by calculating the relative percentage of the area fraction of the O-deficient peak. The percentage of oxygen vacancies of the commercial ZnO NPs was ~36% (Fig. 6(c)). Furthermore, oxygen vacancies of the H_2O_2 treated/annealed ZnO NPs for various concentrations are as follows: ~41% for 0.075 M, ~46% for 0.125 M, ~38 for 0.250 M, and ~37% for 1.000 M. According to the XRD analysis, 0.250 and 1.000 M samples have smaller particles than the rest. Therefore, a larger number of oxygen vacancies is expected due to their higher surface-to-volume ratio.

However, that was not the case (Figs. 6(f) and 6(g)) due to the reduced ZnO phase formation, as revealed in Fig. 2. Particularly, the 0.075 and 0.125 M samples have higher contents of oxygen vacancies than the other two. Specifically, the 0.125 M sample has more vacancies compared with the 0.075 M sample. As described above, the ZnO_2 phase, transformed by H_2O_2 treatment, is easily converted to the more stable ZnO phase at high annealing temperature; however, the converted ZnO NPs have oxygen vacancies on the surface [24]. According to the XRD analysis (Fig. 2), a high content (~85%) of original ZnO NP powders was converted to ZnO NPs using H_2O_2 concentrations of 0.075 and 0.125 M. Therefore, two samples contained a higher content of oxygen-vacant ZnO NPs than the other two (0.250 and 1.000 M). Therefore, the 0.075 and 0.125 M samples have higher contents of oxygen vacancies than the other two. Additionally, the formation of ZnO_2 increased with the increasing concentration of H_2O_2, increasing the amount of oxygen-vacant ZnO. Therefore, the 0.125 M H_2O_2 treated/annealed ZnO NPs have more oxygen vacancies than the 0.075 M sample. Accordingly, the 0.125 M sample can have more oxygen vacancies than the 0.075 M sample. Moreover, the shift of XPS Zn $2p_{3/2}$ peak to lower energy in the 0.075 and 0.125 M samples is undoubtedly attributed to the increased oxygen vacancy.

The analysis of Raman spectra was performed to confirm the existence of oxygen vacancies further. Figure 7 shows the Raman spectra of the commercial ZnO NPs and those of 0.075, 0.125, and 0.250 M H_2O_2 treated/annealed ZnO NPs. Four Raman modes were observed at 331, 381, 440, and 584 cm^{-1}, associated with the ZnO wurtzite structure [38,39]. The sharp and strong peak at 440 cm^{-1} can be assigned to the nonpolar optical phonon E_2 (high) mode [40]. The small peaks at ~331 and 381 cm^{-1} can be attributed to E_2 (high) − E_2 (low) multiphonon scattering phonon mode and A_1 (TO) transverse optical phonon mode, respectively. The polar phonon peaks centered at 584 cm^{-1} represent A_1 (LO) longitudinal optical phonon mode, which is attributed to the defects such as oxygen vacancies [41]. The Raman spectra were normalized with respect to the E_2 (high) − E_2 (low) peak for the ease of interpretation (Fig. 8). The ratio between A_1 (LO) and E_2 (high) peak intensities (I(A_1 (LO))/I(E_2 (high)) indicates the number of oxygen vacancies in the sample [38,39]. The contents of oxygen vacancies increase in the 0.125 M

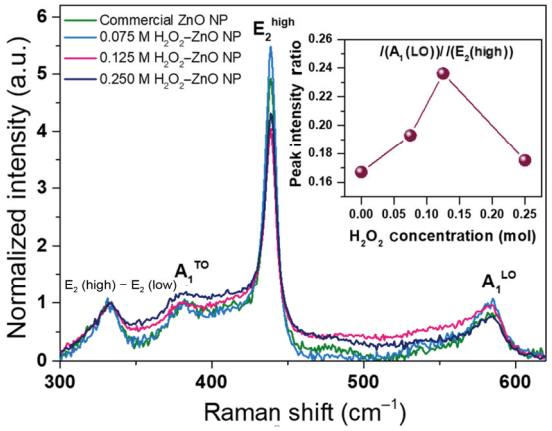

Fig. 7 Raman spectra of commercial ZnO NPs and x M H_2O_2 treated/annealed ZnO NPs (x = 0.075, 0.125, and 0.250).

sample but decrease in the 0.250 M samples (see the inset of Fig. 7). This trend is consistent with the results obtained from the XPS analysis, as shown in Figs. 6(c)–6(g).

We compared the sensing responses of all the prepared samples upon exposure to 10 ppm acetone at the optimal working temperature of 400 ℃ (Fig. 8). The response was ~1070 for the commercial ZnO NPs, ~7359 for 0.075 M, ~27,562 for 0.125 M, ~3068 for 0.250 M, and ~1807 for 1.000 M H_2O_2 treated/annealed ZnO NPs. The relative percentages of the number of oxygen vacancies obtained from the XPS O 1s peak analysis are also shown in Figs. 6(c)–6(g). The sensing response of the samples shows the same trend as that of the number of oxygen vacancies. Oxygen vacancies in the ZnO surface are considered to be the adsorption sites of oxygen species for sensing reaction, and then acetone molecules react to the adsorbed

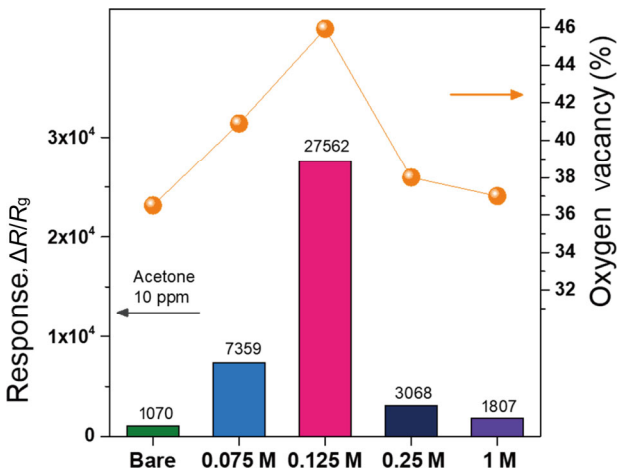

Fig. 8 Overall comparison of responses and fraction of oxygen vacancies.

oxygen species on the ZnO surface. We also confirmed that the ZnO surface covered with oxygen species is more preferred for the adsorption of acetone molecules thermodynamically. This result was obtained from computational calculations, and we discuss more about it in the following. Therefore, a higher sensing response can be explained by the increased number of oxygen vacancies. The H_2O_2 treated/annealed ZnO NPs show a highly improved sensing response than the commercial ZnO NPs, as shown in Fig. 8. In particular, the 0.125 M sample displays the best sensing response. The results reveal that the H_2O_2 treatment and annealing process can easily produce oxygen vacancies on the surface of ZnO NPs. The optimal concentration of H_2O_2 for the best acetone sensing response of ZnO NPs was found to be approximately 0.125 M. Additionally, the highest sensing response value of ~27,562 for acetone 10 ppm is remarkably higher than that of previously reported various acetone sensors based on MOSs [42–54], as shown in Fig. 9. This indicates that controlling the number of oxygen vacancies by H_2O_2 treatment is a very effective way to improve the sensing performance using simple commercial NPs.

Furthermore, we tested other sensing properties, such as sensitivity for other target gases and repeatability for

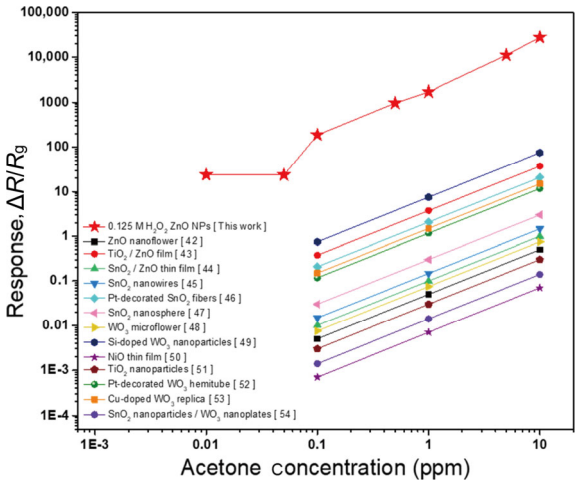

Fig. 9 Comparison of sensing response of 0.125 M H_2O_2 treated/annealed ZnO NPs to previously reported MOS-based gas sensors for various concentrations of acetone.

the detection of acetone, of the 0.125 M H_2O_2 treated/annealed ZnO NPs at its optimal working temperature of 400 ℃. Figure 10(a) shows the response of the sample to various gases, such as acetone, dimethyl methylphosphonate (DMMP), hydrogen sulfide, ethanol, toluene, isoprene, benzene, formaldehyde, methane, hydrogen, CO, and CO_2, at the same concentration of

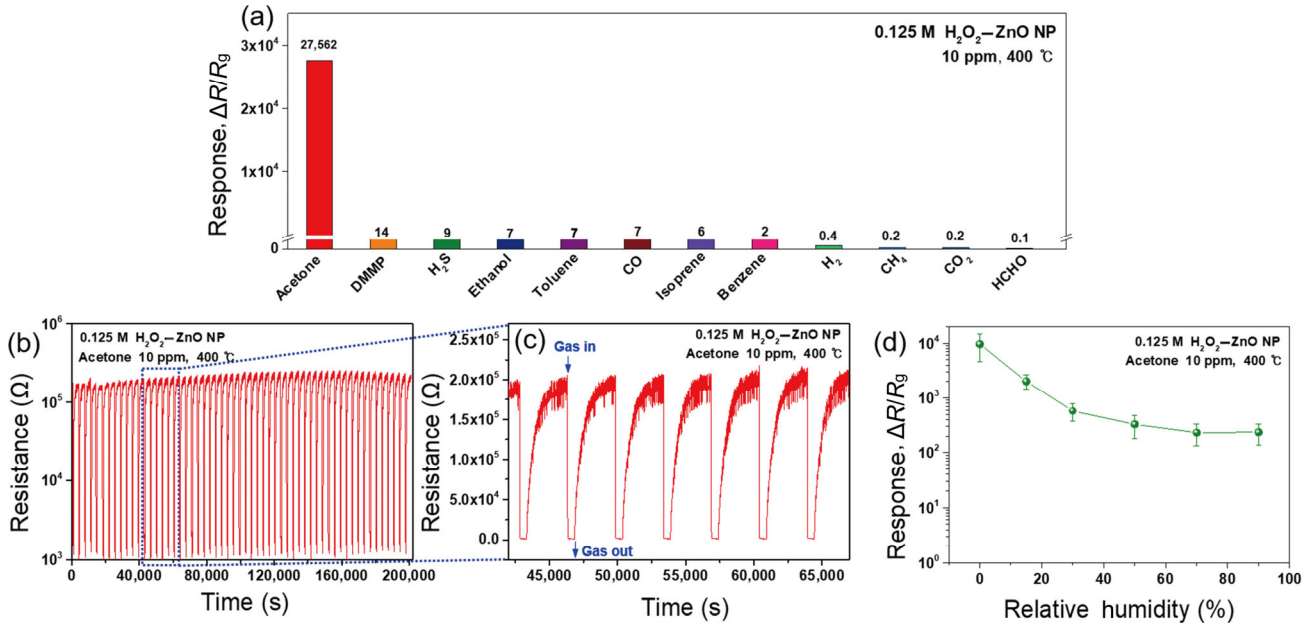

Fig. 10 (a) Sensing response of the 0.125 M H_2O_2 treated/annealed ZnO NPs to various gases, such as acetone, dimethyl methylphosphonate (DMMP), H_2S, ethanol, toluene, CO, isoprene, benzene, H_2, CH_4, CO_2, and HCHO, at the same concentration of 10 ppm and the optimal working temperature of 400 ℃. (b) Reliability of 0.125 M sample for detecting 10 ppm acetone over 60 cycles at 400 ℃; (c) magnified plot of the real-time resistance curves marked by the dotted box in (b). (d) Response change of 0.125 M sample for 10 ppm acetone under different conditions of relative humidity (RH) at 400 ℃.

10 ppm at 400 ℃. The response to acetone was remarkably higher than that of the other gases, indicating that the sensor based on the 0.125 M H_2O_2 treated/annealed ZnO NPs provides a clear distinction during acetone gas detection. Figure 10(b) shows the repeatability of the 0.125 M H_2O_2 treated/annealed ZnO NPs during sensing measurement for the detection of 10 ppm acetone over 60 cycles at 400 ℃. Furthermore, Fig. 10(c) shows the magnified plot of the real-time resistance curves marked by the dotted box in Fig. 10(b). Figures 10(b) and 10(c) clearly show that the sensing resistance is approximately constant throughout 60 cycles of continuous detection of 10 ppm acetone. This implies a good repeatability in the response of the 0.125 M H_2O_2 treated/annealed ZnO NPs for sensing 10 ppm acetone.

We also tested the humidity influence on the sensing response of the 0.125 M H_2O_2 treated/annealed ZnO NPs to detect 10 ppm acetone under different humidity conditions (0–90 RH%). The response decreased due to the contamination of the sensing active sites by the adsorption of water molecules (Fig. 10(d)). We found that the response of the sensor at a dry condition was significantly degraded by two orders of magnitude at 90 RH%. This indicates that the surface defects of the H_2O_2 treated/annealed samples provide a higher sensing response under dry environmental conditions; however, they readily lead to higher adsorption of water molecules under high humidity conditions, resulting in greater contamination of the sensing active sites. Consequently, the response is significantly reduced. However, this disadvantage of humidity interference can be overcome using a moisture filter when this material is applied to a breath analyzer [55].

A possible mechanism for the pristine ZnO and oxygen-vacant ZnO NPs is illustrated in Fig. 11 for the detection of acetone based on the characterization results of surface chemistry. The mechanism is based on the change in the electrical resistance of ZnO during adsorption and desorption of gas molecules on the ZnO surface. When the ZnO NPs are under ambient air, the O_2 molecules in the air are adsorbed on the surface of ZnO NPs, and the adsorbed O_2 molecules take the electrons from the conduction band of the ZnO (Fig. 11(a), left). Subsequently, O^{2-} ions are formed on the ZnO surface at the optimal operating temperature of 400 ℃ in the air (Fig. 11(a), left). Different types of oxygen ion species, such as O_2^-, O^-, and O^{2-}, are formed depending on the working temperature based on Reactions (4)–(6) [56]:

$$O_{2(ads)} + e^- \leftrightarrow O^-_{2(ads)}, T < 100\ ℃ \quad (4)$$

$$O_{2(ads)} + 2e^- \leftrightarrow 2O^-_{(ads)}, 100\ ℃ \leqslant T \leqslant 300\ ℃ \quad (5)$$

$$O^-_{(ads)} + e^- \leftrightarrow O^{2-}_{(ads)}, T > 300\ ℃ \quad (6)$$

These reactions show that an electron depletion layer is formed on the surface of ZnO, resulting in high resistance of the sample (Fig. 11(a), left). When the sample is exposed to acetone (CH_3COCH_3) gas, the gas molecules react with the adsorbed oxygen ion species (O^{2-}). Many electrons are released back to the

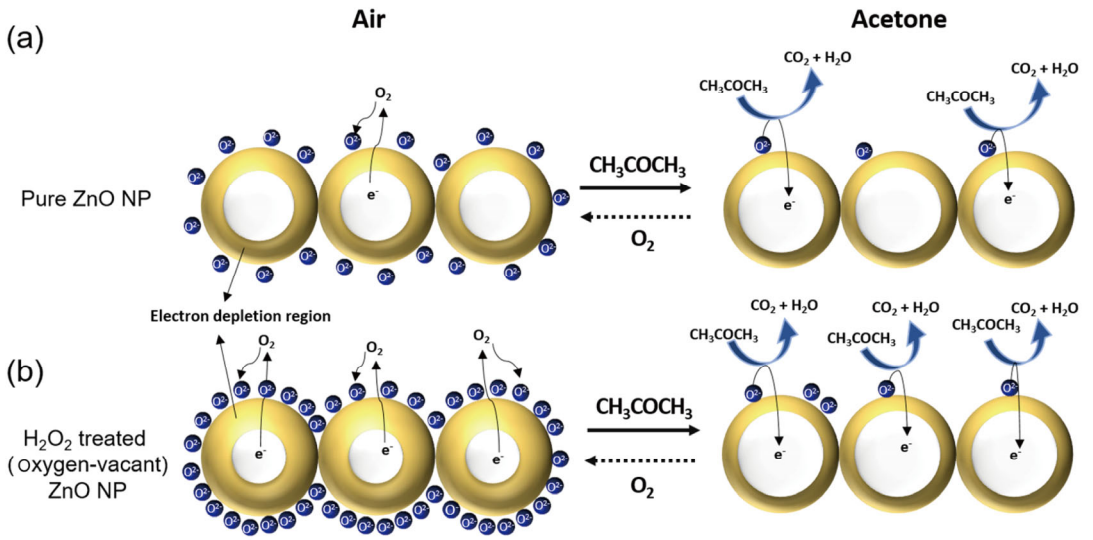

Fig. 11 Schematic illustration of the sensing reaction mechanism of (a) commercial ZnO NPs and (b) H_2O_2 treated/annealed (oxygen-vacant) ZnO NPs in air and acetone.

ZnO conduction band (Fig. 11(a), right), as shown by Reaction (7) [19]. Subsequently, the thickness of the depletion layer decreases, resulting in a decrease in the resistance (Fig. 11(a), right). These resistance change, before and after the chemical reaction of the target gas molecules with oxygen ion species on the sample surface, corresponds to the sensing response.

$$CH_3COCH_{3(ads)} + 8O^{2-}_{(ads)} \rightarrow 3CO_{2(g)} + 3H_2O_{(g)} + 16e^- \quad (7)$$

The oxygen vacancies act as acceptors of oxygen ion species in the air at high temperatures in the case of oxygen-vacant ZnO NPs through H_2O_2 treatment and annealing [29]. Many oxygen ion species are adsorbed, and the thicker depletion layer is generated (Fig. 11(b), left). Therefore, the resistance of oxygen-vacant ZnO NPs in the air becomes higher than that of the untreated ones. Then the adsorbed acetone molecules interact with a greater number of oxygen ion species during the sensing reaction, leading to a significant decrease in resistance. Accordingly, the oxygen-vacant sample exhibited a significantly sensitive and improved acetone gas sensing response.

We further performed density functional theory calculations to elucidate the high sensing response of H_2O_2 treated/annealed ZnO NPs for acetone. The non-polar ZnO($10\bar{1}0$) surface was used as the slab model because it is not only the most stable surface of ZnO [57,58], but also the dominating surface as verified from our XRD results. It is expected that O_2 can be easily adsorbed on the oxygen-vacant ZnO surface due to O_2 molecules those exist in the air under gas-sensing conditions. Therefore, we calculated the dissociative adsorption energy in which O_2 molecules are dissociated on the oxygen-vacant ZnO surface such that one O atom fills the oxygen vacancy site, and the other O atom is adsorbed at the Zn bridge site (Fig. S1 in the ESM). Hence, the O_2 dissociative adsorption on the oxygen-vacant ZnO surface (−1.49 eV) is significantly more favorable than on the clean ZnO surface (+2.96 eV). Therefore, we considered the oxygen-adsorbed ZnO surface model, reflecting the oxygen adsorption under gas-sensing conditions. We constructed the oxygen full-covered ZnO($10\bar{1}0$) surface and calculated the adsorption energy of acetone, ethanol, and methane on the oxygen full-covered ZnO surface to describe the oxygen-adsorbed ZnO surface in gas molecule sensing conditions. The adsorption energies of acetone, ethanol, and methane were calculated using Eq. (8):

$$\Delta E_{ads} = E_{molecule+slab} - (E_{slab} + E_{molecule}) \quad (8)$$

where ΔE_{ads} denotes the adsorption energy, $E_{molecule+slab}$ represents the total energy of surface and adsorbed molecule, E_{slab} is the total energy of the surface, and $E_{molecule}$ denotes the total energy of an isolated molecule. The optimized adsorption configurations of acetone, ethanol, and methane on the oxygen full-covered ZnO($10\bar{1}0$) surface are depicted in Fig. 12(a), and their adsorption energies are plotted in Fig. 12(b). The adsorption energies reveal that ethanol (−0.35 eV) and methane (−0.03 eV) can be considered as weak physisorption; however, acetone is most strongly adsorbed on the ZnO surface (−1.47 eV). In the adsorption configuration of acetone, pre-adsorbed oxygen (dark-red) of the ZnO surface binds to carbonyl C atom of acetone when carbonyl O atom (red) of acetone binds to Zn atom at the surface. This bidentate adsorption configuration is thermodynamically favorable for acetone on the oxygen full-covered ZnO($10\bar{1}0$) surface, compared to other weakly physisorbed molecules.

Additionally, we calculated the adsorption energies on the ZnO surface with different contents of pre-adsorbed oxygen—oxygen-vacant surface, clean surface, one oxygen atom-adsorbed surface, and oxygen full-covered surface—to explain the effect of pre-adsorbed oxygen on the adsorption strength at the ZnO surface. The results of the calculation are presented in Fig. 12(c). The adsorption energies of ethanol on the oxygen-vacant ZnO and clean ZnO surfaces (black and orange bars) were −0.73 and −1.00 eV, respectively, which were stronger than those of acetone (−0.45 and −0.58 eV). In this case, ethanol forms not only the bonds between hydroxyl O atom and surface Zn atom but also the hydrogen bonding between hydroxyl H atom and lattice O atom. However, acetone (−1.31 eV) binds more strongly on the ZnO surface in one oxygen-adsorbed ZnO surface (blue bar) with bidentate configuration bonding between carbonyl C of acetone and pre-adsorbed O on the ZnO surface. This difference in adsorption configuration between the clean and oxygen pre-adsorbed surfaces of acetone makes it more favorable to be adsorbed on the ZnO surface with pre-adsorbed oxygen. In the case of methane adsorption, all ZnO surfaces show the weak physisorption of methane. Acetone is most favorable to be bound on the ZnO surface with pre-adsorbed oxygen among the three gas molecules due to the adsorption energies on different ZnO surfaces.

The surface of oxygen-vacant ZnO NPs can be covered with the large number of oxygen ion species,

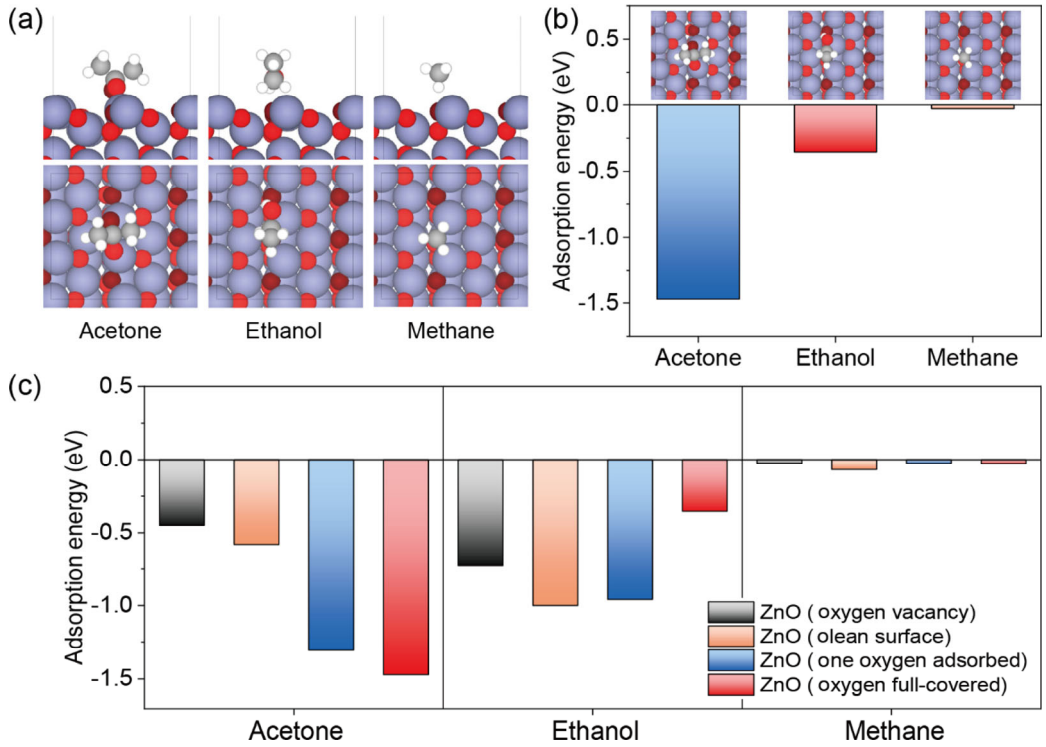

Fig. 12 (a) Optimized adsorption configurations of acetone, ethanol, and methane on oxygen ion species full-covered ZnO($10\bar{1}0$) surface in the cross-section view (upper panel) and the top section view (lower panel). Zn, lattice O, adsorbed O, C, and H atoms are shown as medium-purple, red, dark-red, grey, and white spheres, respectively. (b) Plot of adsorption energy (ΔE_{ads}) corresponds to each configuration of (a). (c) ΔE_{ads} plot of each gas molecule on the ZnO depending on the various surface conditions: oxygen-vacant surface, clean surface, one oxygen-adsorbed surface, and oxygen full-covered surface.

as mentioned in the sensing mechanism part of Fig. 11. Therefore, highly enhanced sensing response of 0.125 M H_2O_2 treated/annealed ZnO NPs than that of bare ZnO NPs (Fig. 8) is attributed to the higher adsorption energy of acetone molecules, especially in the oxygen full-covered ZnO surface due to the bidentate configuration bonding between carbonyl C of acetone and pre-adsorbed O on the ZnO surface, as described by the simulation (Fig. 12(c)). Furthermore, the remarkably high response of the 0.125 M H_2O_2 treated/annealed ZnO NPs to acetone than other gases, such as ethanol and methane (Fig. 10(a)), is explained by significantly higher adsorption energies of acetone than those of ethanol and methane (Fig. 12(b)).

4 Conclusions

We show that only a simple H_2O_2 treatment and annealing process can significantly improve the acetone sensing performance of the commercial ZnO NPs by creating abundant oxygen vacancies on the surface of ZnO NPs. The ZnO NPs, annealed after surface treatment with an optimized H_2O_2 content of 0.125 M, exhibited a significantly higher sensing response of ~27,562 to 10 ppm acetone at the optimal working temperature of 400 ℃ compared with the untreated commercial ZnO NPs. Moreover, this value is remarkably higher than that reported so far for various acetone sensors based on MOSs. The surface defect of oxygen vacancies was verified by analyzing surface chemistry using XPS and Raman spectroscopy. Therefore, the significantly high response of the 0.125 M sample can be attributed to the generation of many oxygen vacancies on the surface of ZnO NPs. Consequently, we developed a highly sensitive acetone sensor based on ZnO with a simple surface treatment. In addition, first-principles calculations indicate that pre-adsorbed O formed on the surface of H_2O_2 treated ZnO NPs can provide a favorable adsorption energy, especially for acetone detection, due to strong bidentate bonding between carbonyl C atom of acetone molecules and pre-adsorbed O on the ZnO surface. Our study demonstrates that the control of surface oxygen vacancies by H_2O_2 treatment is an effective method to improve the sensing response significantly. Furthermore, the surface

treatment method can be adopted to other commercial MOS NPs without the complicated material synthesis process, reducing the manufacturing time of sensor devices and enabling large-scale fabrication.

Acknowledgements

This research was supported by the Technology Innovation Program (No. 20013621, Center for Super Critical Material Industrial Technology) funded by the Ministry of Trade, Industry & Energy (MOTIE, Republic of Korea), the Priority Research Centers Program (2019R1A6A1A11 055660), and the Basic Science Research Program (2017 M3A9F1052297) through the National Research Foundation of Korea (NRF), funded by the Republic of Korean Government (Ministry of Science and ICT). Jong Hyeok PARK acknowledges the support from the International Energy Joint R&D Program of the Korea Institute of Energy Technology Evaluation and Planning (KETEP), granted financial resource from the Ministry of Trade, Industry & Energy, Republic of Korea (20208510010310). Hyun-Sook LEE gratefully acknowledges the support from the Basic Research in Science and Engineering Program of the NRF (2021R1A2C1013690).

Electronic Supplementary Material

Supplementary material is available in the online version of this article at https://doi.org/10.1007/s40145-022-0570-x.

References

[1] Amiri V, Roshan H, Mirzaei A, *et al*. Nanostructured metal oxide-based acetone gas sensors: A review. *Sensors* 2020, **20**: 3096.
[2] Jia QQ, Ji HM, Zhang Y, *et al*. Rapid and selective detection of acetone using hierarchical ZnO gas sensor for hazardous odor markers application. *J Hazard Mater* 2014, **276**: 262–270.
[3] Šetka M, Bahos FA, Matatagui D, *et al*. Love wave sensors with silver modified polypyrrole nanoparticles for VOCs monitoring. *Sensors* 2020, **20**: 1432.
[4] Do JS, Wang SH. On the sensitivity of conductimetric acetone gas sensor based on polypyrrole and polyaniline conducting polymers. *Sens Actuat B Chem* 2013, **185**: 39–46.
[5] Deng CH, Zhang J, Yu XF, *et al*. Determination of acetone in human breath by gas chromatography–mass spectrometry and solid-phase microextraction with on-fiber derivatization. *J Chromatogr B* 2004, **810**: 269–275.
[6] Neri G, Bonavita A, Micali G, *et al*. Design and development of a breath acetone MOS sensor for ketogenic diets control. *IEEE Sens J* 2010, **10**: 131–136.
[7] Kupari M, Lommi J, Ventilä M, *et al*. Breath acetone in congestive heart failure. *Am J Cardiol* 1995, **76**: 1076–1078.
[8] Marcondes-Braga FG, Gutz IGR, Batista GL, *et al*. Exhaled acetone as a new biomarker of heart failure severity. *Chest* 2012, **142**: 457–466.
[9] Anderson JC. Measuring breath acetone for monitoring fat loss: Review. *Obesity (Silver Spring)* 2015, **23**: 2327–2334.
[10] Rashid TR, Phan DT, Chung GS. A flexible hydrogen sensor based on Pd nanoparticles decorated ZnO nanorods grown on polyimide tape. *Sens Actuat B Chem* 2013, **185**: 777–784.
[11] Yu X, Song F, Zhai B, *et al*. Electrospun ZnO nanotubes and its gas sensing applications. *Phys E Low Dimensional Syst Nanostructures* 2013, **52**: 92–96.
[12] Khan SB, Faisal M, Rahman MM, *et al*. Low-temperature growth of ZnO nanoparticles: Photocatalyst and acetone sensor. *Talanta* 2011, **85**: 943–949.
[13] Al-Hardan NH, Abdullah MJ, Aziz AA. Performance of Cr-doped ZnO for acetone sensing. *Appl Surf Sci* 2013, **270**: 480–485.
[14] Darvishnejad MH, Anaraki Firooz A, Beheshtian J, *et al*. Highly sensitive and selective ethanol and acetone gas sensors by adding some dopants (Mn, Fe, Co, Ni) onto hexagonal ZnO plates. *RSC Adv* 2016, **6**: 7838–7845.
[15] Wang LW, Wang SR, Xu MJ, *et al*. A Au-functionalized ZnO nanowire gas sensor for detection of benzene and toluene. *Phys Chem Chem Phys* 2013, **15**: 17179–17186.
[16] Koo A, Yoo R, Woo SP, *et al*. Enhanced acetone-sensing properties of Pt-decorated Al-doped ZnO nanoparticles. *Sens Actuat B Chem* 2019, **280**: 109–119.
[17] Zhu L, Zeng W. Room-temperature gas sensing of ZnO-based gas sensor: A review. *Sens Actuat A Phys* 2017, **267**: 242–261.
[18] Zhang LX, Yin YY. Large-scale synthesis of flower-like ZnO nanorods via a wet-chemical route and the defect-enhanced ethanol-sensing properties. *Sens Actuat B Chem* 2013, **183**: 110–116.
[19] Zhang LX, Zhao JH, Lu HQ, *et al*. High sensitive and selective formaldehyde sensors based on nanoparticle-assembled ZnO micro-octahedrons synthesized by homogeneous precipitation method. *Sens Actuat B Chem* 2011, **160**: 364–370.
[20] Chen M, Wang ZH, Han DM, *et al*. Porous ZnO polygonal nanoflakes: Synthesis, use in high-sensitivity NO_2 gas sensor, and proposed mechanism of gas sensing. *J Phys Chem C* 2011, **115**: 12763–12773.
[21] Ahn MW, Park KS, Heo JH, *et al*. Gas sensing properties of defect-controlled ZnO-nanowire gas sensor. *Appl Phys Lett* 2008, **93**: 263103.
[22] Wang JP, Wang ZY, Huang BB, *et al*. Oxygen vacancy induced band-gap narrowing and enhanced visible light photocatalytic activity of ZnO. *ACS Appl Mater Interfaces* 2012, **4**: 4024–4030.
[23] Li XM, Song JZ, Liu YL, *et al*. Controlling oxygen vacancies and properties of ZnO. *Curr Appl Phys* 2014, **14**: 521–527.
[24] Kim WS, Choi M, Yong K. Generation of oxygen vacancies in ZnO nanorods/films and their effects on gas sensing properties. *Sens Actuat B Chem* 2015, **209**: 989–996.
[25] Kresse G. *Ab initio* molecular dynamics for liquid metals. *J Non Cryst Solids* 1995, **192–193**: 222–229.
[26] Kresse G, Furthmüller J. Efficient iterative schemes for *ab initio* total-energy calculations using a plane-wave basis set. *Phys Rev B Condens Matter* 1996, **54**: 11169–11186.

[27] Blöchl PE. Projector augmented-wave method. *Phys Rev B Condens Matter* 1994, **50**: 17953–17979.
[28] Kresse G, Joubert D. From ultrasoft pseudopotentials to the projector augmented-wave method. *Phys Rev B* 1999, **59**: 1758–1775.
[29] Perdew JP, Burke K, Ernzerhof M. Generalized gradient approximation made simple. *Phys Rev Lett* 1996, **77**: 3865–3868.
[30] Monkhorst HJ, Pack JD. Special points for Brillouin-zone integrations. *Phys Rev B* 1976, **13**: 5188–5192.
[31] Abrahams SC, Bernstein JL. Remeasurement of the structure of hexagonal ZnO. *Acta Crystallogr Sect B* 1969, **B25**: 1233–1236.
[32] Halder NC, Wagner CNJ. Separation of particle size and lattice strain in integral breadth measurements. *Acta Cryst* 1966, **20**: 312–313.
[33] Izumi F, Ikeda T. Implementation of the Williamson–Hall and Halder–Wagner methods into RIETAN-FP. In: *Annual Report Advanced Ceramics Research Center Nagoya Institute of Technology*. Nagoya, Japan: Annual report of the Advanced Ceramics Research Center Nagoya Institute of Technology 2014, **3**: 33–38.
[34] Canchanya-Huaman Y, Mayta-Armas AF, Pomalaya-Velasco J, *et al*. Strain and grain size determination of CeO_2 and TiO_2 nanoparticles: Comparing integral breadth methods versus rietveld, μ-Raman, and TEM. *Nanomaterials* 2021, **11**: 2311.
[35] Geng ZG, Kong XD, Chen WW, *et al*. Oxygen vacancies in ZnO nanosheets enhance CO_2 electrochemical reduction to CO. *Angew Chem Int Ed* 2018, **57**: 6054–6059.
[36] Wang JF, Li Y, Kong Y, *et al*. Non-fluorinated superhydrophobic and micro/nano hierarchical Al doped ZnO film: The effect of Al doping on morphological and hydrophobic properties. *RSC Adv* 2015, **5**: 81024–81029.
[37] Gan JY, Lu XH, Wu JH, *et al*. Oxygen vacancies promoting photoelectrochemical performance of In_2O_3 nanocubes. *Sci Rep* 2013, **3**: 1021.
[38] Momot A, Amini MN, Reekmans G, *et al*. A novel explanation for the increased conductivity in annealed Al-doped ZnO: An insight into migration of aluminum and displacement of zinc. *Phys Chem Chem Phys* 2017, **19**: 27866–27877.
[39] Russo V, Ghidelli M, Gondoni P, *et al*. Multi-wavelength Raman scattering of nanostructured Al-doped zinc oxide. *J Appl Phys* 2014, **115**: 073508.
[40] Yang YH, Wang CX, Wang B, *et al*. Radial ZnO nanowire nucleation on amorphous carbons. *Appl Phys Lett* 2005, **87**: 183109.
[41] Yang L, Tang YH, Hu AP, *et al*. Raman scattering and luminescence study on arrays of ZnO doped with Tb^{3+}. *Phys B Condens Matter* 2008, **403**: 2230–2234.
[42] Huang JR, Wu YJ, Gu CP, *et al*. Large-scale synthesis of flowerlike ZnO nanostructure by a simple chemical solution route and its gas-sensing property. *Sens Actuat B Chem* 2010, **146**: 206–212.
[43] Zhu BL, Xie CS, Wang WY, *et al*. Improvement in gas sensitivity of ZnO thick film to volatile organic compounds (VOCs) by adding TiO_2. *Mater Lett* 2004, **58**: 624–629.
[44] Kim KW, Cho PS, Kim SJ, *et al*. The selective detection of C_2H_5OH using SnO_2–ZnO thin film gas sensors prepared by combinatorial solution deposition. *Sens Actuat B Chem* 2007, **123**: 318–324.
[45] Qin LP, Xu JQ, Dong XW, *et al*. The template-free synthesis of square-shaped SnO_2 nanowires: The temperature effect and acetone gas sensors. *Nanotechnology* 2008, **19**: 185705.
[46] Shin JW, Choi SJ, Lee IK, *et al*. Thin-wall assembled SnO_2 fibers functionalized by catalytic Pt nanoparticles and their superior exhaled-breath-sensing properties for the diagnosis of diabetes. *Adv Funct Mater* 2013, **23**: 2357–2367.
[47] Xu J, Li YS, Huang HT, *et al*. Synthesis, characterizations and improved gas-sensing performance of SnO_2 nanospike arrays. *J Mater Chem* 2011, **21**: 19086–19092.
[48] Huang JR, Xu XJ, Gu CP, *et al*. Large-scale synthesis of hydrated tungsten oxide 3D architectures by a simple chemical solution route and their gas-sensing properties. *J Mater Chem* 2011, **21**: 13283–13289.
[49] Righettoni M, Tricoli A, Pratsinis SE. Si:WO_3 sensors for highly selective detection of acetone for easy diagnosis of diabetes by breath analysis. *Anal Chem* 2010, **82**: 3581–3587.
[50] Lee CY, Chiang CM, Wang YH, *et al*. A self-heating gas sensor with integrated NiO thin-film for formaldehyde detection. *Sens Actuat B Chem* 2007, **122**: 503–510.
[51] Rella R, Spadavecchia J, Manera MG, *et al*. Acetone and ethanol solid-state gas sensors based on TiO_2 nanoparticles thin film deposited by matrix assisted pulsed laser evaporation. *Sens Actuat B Chem* 2007, **127**: 426–431.
[52] Choi SJ, Lee IK, Jang BH, *et al*. Selective diagnosis of diabetes using Pt-functionalized WO_3 hemitube networks as a sensing layer of acetone in exhaled breath. *Anal Chem* 2013, **85**: 1792–1796.
[53] Zhu SM, Liu XY, Chen ZX, *et al*. Synthesis of Cu-doped WO_3 materials with photonic structures for high performance sensors. *J Mater Chem* 2010, **20**: 9126–9132.
[54] Nayak AK, Ghosh R, Santra S, *et al*. Hierarchical nanostructured WO_3–SnO_2 for selective sensing of volatile organic compounds. *Nanoscale* 2015, **7**: 12460–12473.
[55] Van den Broek J, Weber IC, Güntner AT, *et al*. Highly selective gas sensing enabled by filters. *Mater Horiz* 2021, **8**: 661–684.
[56] Ahmad MZ, Sadek AZ, Latham K, *et al*. Chemically synthesized one-dimensional zinc oxide nanorods for ethanol sensing. *Sens Actuat B Chem* 2013, **187**: 295–300.
[57] Wöll C. The chemistry and physics of zinc oxide surfaces. *Prog Surf Sci* 2007, **82**: 55–120.
[58] Goclon J, Meyer B. The interaction of H_2S with the ZnO(1010) surface. *Phys Chem Chem Phys* 2013, **15**: 8373–8382.